

# Study on crystallographic and electronic structure of micrometre-scale ZnO and ZnO:B rods via X-ray absorption fine-structure spectroscopy

Selma Erat,<sup>a,b,\*</sup> Osman Murat Ozkendir,<sup>c,\*</sup> Saadet Yildirimcan,<sup>b</sup> Selen Gunaydin,<sup>c</sup> Messaoud Harfouche,<sup>d</sup> Bunyamin Demir,<sup>b,e</sup> and Artur Braun<sup>f</sup>

Received 19 August 2020

Accepted 3 December 2020

Edited by U. Jeng, NSRRC, Taiwan

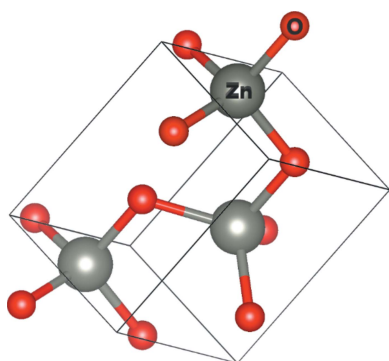
**Keywords:** semiconductors; electronic structure; crystallographic structure; X-ray absorption spectroscopy; ZnO.

<sup>a</sup>Vocational School of Technical Sciences, Department of Medical Services and Techniques, Program of Opticianry, Mersin University, Mersin 33340, Turkey, <sup>b</sup>Advanced Technology Education, Research and Application Center, Mersin University, Mersin 33340, Turkey, <sup>c</sup>Faculty of Technology, Energy Systems Engineering, Tarsus University, Tarsus 33400, Turkey, <sup>d</sup>Synchrotron Light for Experimental Science and Applications in the Middle East (SESAME), Allan 19252, Jordan, <sup>e</sup>Faculty of Engineering, Department of Mechanical Engineering, Mersin University, Mersin 33340, Turkey, and <sup>f</sup>Laboratory for High Performance Ceramics, Empa – Swiss Federal Laboratories for Materials Science and Technology, CH-8600 Dübendorf, Switzerland. \*Correspondence e-mail: selma.erat@mersin.edu.tr, ozkendir@gmail.com

X-ray absorption near-edge structure (XANES) and extended X-ray absorption fine-structure (EXAFS) spectra were recorded to investigate the electronic structure and local crystal structure of ZnO and ZnO:B powders produced via hydrothermal synthesis. ZnO and ZnO:B grow as micrometre-scale rods with hexagonal shape, as confirmed by scanning electron microscopy micrographs. The number of broken ZnO:B rods increases with increasing B concentration, as observed in the images, due to B atoms locating in between the Zn and O atoms which weakens and/or breaks the Zn–O bonds. However, no disorder within the crystallographic structure of ZnO upon B doping is observed from X-ray diffraction results, which were supported by EXAFS results. To determine the atomic locations of boron atoms in the crystal structure and their influence on the zinc atoms, EXAFS data were fitted with calculated spectra using the crystal structure parameters obtained from the crystallographic analysis of the samples. EXAFS data fitting and complementary *k*-weight analysis revealed the positions of the B atoms – their positions were determined to be in between the Zn and O atoms.

## 1. Introduction

Zinc oxide (ZnO) is a direct wide-band-gap group II–VI semiconductor and has a convergence of electronic and chemical properties. Thus, ZnO is one of the more widely used metal oxides with applications in quite different fields ranging from electronics to catalysis, energy to cosmetics, and fungicides to phosphor (Meyers *et al.*, 2008). For instance, owing to its band gap of 3.37 eV (Wang, Ai & Yu, 2017; Norton, 2004) at room temperature (RT) and high exciton binding energy of 60 meV (Wang, Ai & Yu, 2017; Look *et al.*, 1999) at RT, ZnO is suitable for fabrication of ultra-violet (UV) detectors, UV and blue light emitting devices (Du *et al.*, 2009; Bagnall *et al.*, 1998), and flat panel displays (Zargar Shoushtari *et al.*, 2017; Ellmer & Fiechter, 2008; El-Hilo *et al.*, 2009; Law *et al.*, 2005; Martinson *et al.*, 2007; Kuthirummal *et al.*, 2016; Pawar *et al.*, 2009) and gas sensors (Heiland, 1981; Wang, Yang *et al.*, 2017) *etc.* ZnO was also the first metal oxide to be used as photo-electrode support for dye sensitized solar cells (Baur & Neuweiler, 1927; Allisson, 1930; Tributsch, 1968, 1969). In the past decades, ZnO has been extensively studied and it was found that ZnO mainly occurs in wurtzite crystal structure and



has a hexagonal unit cell with space group notation of  $P6_3mc$  (sketched in Fig. 1) (Momma & Izumi, 2011).

It is well known that the physical properties of materials, particularly nanosized materials, are affected by particle size and/or shape as well as dopant element and doping concentration (Erat & Yildirimcan, 2019a,b; Romeiro *et al.*, 2015). Doping can alter the equilibrium shape of crystals and thus their properties and functions. For example, doping ZnO with transition metals such as Mn, Fe, Co, Ni and Cu modifies the photocatalytic activities of ZnO to reduce the band gap energy (Saleh & Djaja, 2014). Further, it was reported that the electrical properties of ZnO can be enhanced by using elements from group IIIA (*e.g.* B, Al, Ga and In) (Tsay & Hsu, 2013). In this group,  $B^{3+}$  has the lowest ionic radius (0.23 Å) and the highest electronegativity (2.04, Pauling), and the Lewis acid strength of  $B^{3+}$  (10.7) is higher than that of  $Al^{3+}$  (3.04). Because of such properties, B is an effective element for tuning the physical properties of ZnO (Tsay & Hsu, 2013; Tahar & Tahar, 2005). B-doped ZnO has received much attention over the last ten years due to its potential applications in the field of transparent conductive oxides and dilute magnetic semiconductors (Pawar *et al.*, 2009; Tahar & Tahar, 2005; Steinhäuser *et al.*, 2007, 2008; Xu *et al.*, 2010). The accurate determination of the location of dopants is important for the explanation of the dopant effect on the properties of the parental materials (Tsuzuki *et al.*, 2019). While X-ray diffraction (XRD) is the standard method for the determination of the crystallographic structure and phase of bulk materials, doping studies can be challenging for XRD when submicrometre-size particles are to be investigated (Jeong *et al.*, 2008). For study of the electronic structure, local order and conformation of the dopant ion B with respect to the host material ZnO, we resort to synchrotron radiation based X-ray absorption spectroscopy (XAS). For the XAS we consider two parts: near-edge X-ray absorption fine structure (XANES) and extended X-ray absorption fine structure (EXAFS), which are useful techniques to characterize both electronic structure and local structural properties of materials (Braun, 2017; Ankudinov & Rehr, 1997). There are few studies on the local structural properties of ZnO nanoparticles determined via

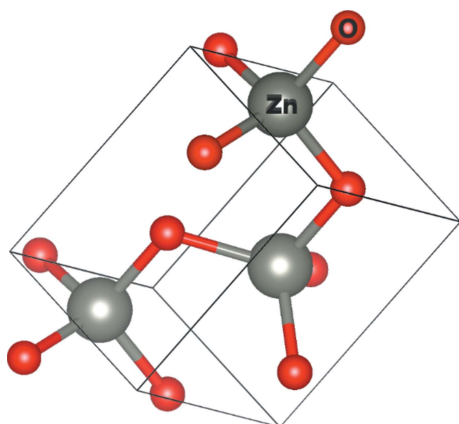


**Figure 1**  
The wurtzite ZnO hexagonal close-packed crystal structure (Momma & Izumi, 2011).

the EXAFS technique, which describes the bonding lengths, bonding length disorders, coordination and atomic species of neighboring atoms around a probe atom (Jeong *et al.*, 2008). Chiou *et al.* (2004a) worked on the electronic structure of ZnO nanorods by angle-dependent X-ray absorption spectroscopy at the oxygen (O)  $K$ -edge and zinc (Zn)  $L_{3-}$  and  $K$ -edges. Further, Chiou *et al.* (2004b) investigated the diameter dependence of the electronic structure of ZnO nanorods using the XANES technique at the O  $K$ -edge and Zn  $L_{3-}$  and  $K$ -edges. The differences between the XANES (Zn  $K$ -edge and O  $K$ -edge) for ZnO nanostructures and ZnO bulk were compared with the theoretically calculated spectra for ZnO surfaces and bulk, and it was concluded that the difference in the XANES was mainly due to local geometry differences around the photoabsorbing sites (Šipr & Rocca, 2011). Recently, the activity of B in inactive  $Li_2MnO_3$  cathode material has been investigated by some of us using XRD and XAFS techniques (Ozkendir *et al.*, 2019).

In the present study, we investigate the electronic structure and local crystal structure of pure and B-doped ZnO synthesized by the hydrothermal method, using XRD, XANES and EXAFS spectroscopy. The morphology of the samples was determined by field-emission scanning electron microscopy (FE-SEM). The atomic distances from the Zn atom are calculated and presented in detail. The atomic position of the B atom in the structure is determined by  $k$ -weight analysis.

## 2. Experimental

ZnO powders were produced by hydrothermal synthesis (Baruah & Dutta, 2009) using zinc nitrate hexahydrate [ $Zn(NO_3)_2 \cdot 0.6H_2O$ ; Sigma-Aldrich], polyethylene glycol (PEG300; Aldrich Chemistry) and ammonia ( $NH_3$ ; Carlo Erba) following a similar procedure to Yildirimcan *et al.* (2016). 0.1 M  $Zn(NO_3)_2 \cdot 0.6H_2O$  was dissolved in 100 ml of distilled water, and then 3.36 g PEG300 was added to the solution. The zinc nitrate is used as a source of  $Zn^{2+}$  and ammonia is used for adjusting the pH of the solution (pH: 10). The resulting solution was further processed at 80°C for 12 h. In order to produce B-doped ZnO, the same procedure is followed using boric acid ( $H_3BO_3$ ) as a source of  $B^{3+}$ .  $H_3BO_3$  was dissolved in ultra-distilled water at certain ratios. 1 ml of the B solution was added to the pure ZnO precursor solution for various weight/volume (w/v, %) concentrations, *e.g.* 2.5%, 3.5%, 5% and 10%. The resulting solution was mixed, and synthesized at the same temperature and dwelling time. The precipitations were firstly filtered and secondly washed using ultra-distilled water, and finally dried in an oven at 80°C for 1 h. The samples are tagged within the text as X1 (undoped ZnO), X2 (2.5%), X3 (3.5%), X4 (5%) and X5 (10% B-doped ZnO).

The X-ray diffraction patterns were recorded at ambient temperature with a Rigaku SmartLab X-ray diffractometer using Cu  $K\alpha$  radiation (1.54059 Å) within the  $2\theta$  range 20°–80°. The morphology of the samples was investigated by FE-SEM (Zeiss-Supra 55). The XANES and XAFS spectra of ZnO and ZnO:B were collected at the XAFS/XRF beamline

at SESAME (Synchrotron-light for Experimental Science and Applications in the Middle East), a third-generation synchrotron light source located in Allan, Jordan. XAFS/XRF is one of the Phase One beamlines at SESAME that has recently become operational (Harfouche *et al.*, 2018). The beamline is optimized for hard X-rays covering the energy range between 4.5 keV and 30 keV and dedicated for X-ray spectroscopic studies in all fields. All of the XAFS data of ZnO and ZnO:B were collected in transmission mode at ambient temperature.

### 3. Computational details

In order to analyze the spectroscopic data in detail, the *ATHENA* and *ARTEMIS* programs were used (Ravel, 2001; Ravel & Newville, 2005). For quantitative EXAFS data analysis, one needs to compare the experimental spectra with the theoretically calculated one by using the commercial *FEFF 8.20* code which is based on the absorption process (Ankudinov & Rehr, 1997). The calculations were performed for 10 Å-thick molecular clusters for the wurtzite ZnO material and the input file was generated with the *ATOMS* program in the *IFEFIT* package (Ravel, 2001). The crystal structure parameters determined from the XRD pattern analysis were used during the input file generation. The wurtzite ZnO cluster containing 340 atoms (Zn, O) was created in close-packed hexagonal geometry and space group *P6<sub>3</sub>mc*. Calculations were used for fitting processes during the data analysis.

### 4. Results and discussion

The crystallographic phase of pure and B-doped ZnO powders was determined by XRD. Fig. 2 shows the X-ray diffractograms of the samples depending on the B concentration.

It is obvious that the patterns of the pure and boron-substituted ZnO samples are quite similar to each other. The

diffraction peaks are in accordance with our previous study (Yildirimcan *et al.*, 2016) and consistent with the results in the standard card (JCPDS no: 36-1451) that confirms that the samples are created in unique wurtzite crystal structure with space group *P6<sub>3</sub>mc* (186). In other words, all of the ZnO:B samples still preserve the ZnO structure as hexagonal wurtzite structure. The XRD peaks are labeled as (100), (002), (101), (102), (110), (103), (200), (112), (201), (004) and (202) at  $2\theta = 31.77^\circ, 34.42^\circ, 36.25^\circ, 47.54^\circ, 56.60^\circ, 62.86^\circ, 66.38^\circ, 67.96^\circ, 69.10^\circ, 72.56^\circ$  and  $76.95^\circ$ , respectively. No other secondary phase has been observed in the XRD patterns in Fig. 2. For instance,  $B_2O_3$  has a strongest peak at  $2\theta = 27.77^\circ$  and another strong peak at  $2\theta = 39.86^\circ$  (JCPDS no: 06-0297). The XRD diffractograms of X1–X5 do not include any peaks at those  $2\theta$  values which confirms that B atoms have been incorporated into the ZnO lattice.

The (101) direction is the most preferred direction for X1 (pure ZnO), X2 and X3. The preferred direction changes to (100) upon increasing the B concentration for samples X4 and X5. Fig. 2(b) shows the enlarged (100) peak of the XRD diffractograms of X1–X5 which definitely displays the shift towards lower angle upon B concentration increase. The shift is calculated by taking into account  $2\theta = 31.95^\circ$  for the parent ZnO as reference. The shift in  $2\theta$  towards lower angle is  $0.1294^\circ, 0.1975^\circ, 0.3192^\circ$  and  $0.2673^\circ$  for X2, X3, X4 and X5, respectively. The average crystallite size of the samples was calculated following Scherrer's formula and the lattice parameters of ZnO and ZnO:B were calculated using the relations given in detail by Yildirimcan *et al.* (2016). The crystallite size values calculated for the (100) peak are 36.0 nm, 37.55 nm, 36.40 nm, 36.20 nm and 35.20 nm for X1, X2, X3, X4 and X5, respectively. The lattice parameters of the ZnO and ZnO:B samples are listed in Table 1 depending on B concentration along with sample codes to make it easier for the reader.

The lattice parameters of ZnO are  $a = 3.2310 \text{ \AA}$  and  $c = 5.2763 \text{ \AA}$  for hexagonal wurtzite structure. Upon B doping, the lattice parameters slightly change and the crystallite size

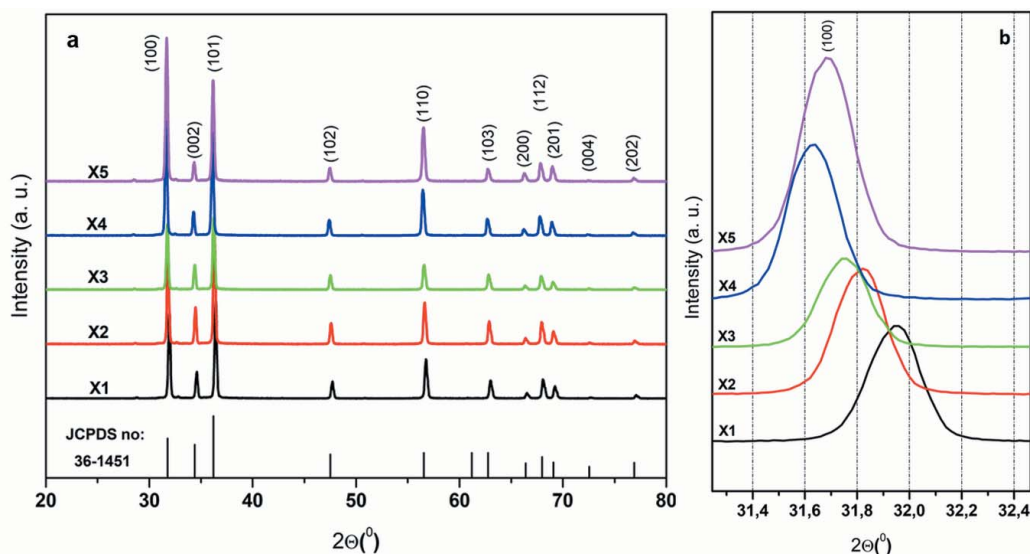


Figure 2 (a) XRD patterns of the parent ZnO and ZnO:B samples. (b) Enlarged (100) peak of the XRD diffractograms.

**Table 1**  
Lattice parameters  $a$  and  $c$  of ZnO and ZnO:B.

Sample code	$a$ (Å)	$c$ (Å)
X1	3.2310	5.2763
X2	3.2434	5.2965
X3	3.2504	5.3079
X4	3.2621	5.3269
X5	3.2570	5.3187

decreases to 35.20 nm for sample X5 (Núñez-Salas *et al.*, 2019; Senol *et al.*, 2015; Kumar *et al.*, 2011).

The morphology of the ZnO and B-doped ZnO samples was investigated by FE-SEM as illustrated in Fig. 3. The ZnO particles grow in a hexagonal shape and resulted in micrometre-scale rods; the tips of the rods tapering into needle shapes with smooth surface. Other groups also observed such

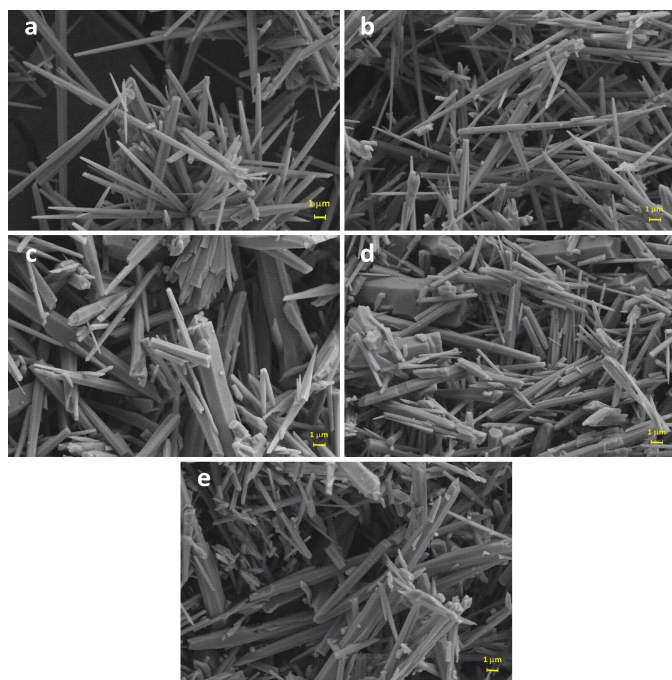


**Figure 3**  
FE-SEM micrographs of ZnO and B-doped ZnO. (a)–(e) X1–X5.

micrometre-scale rods of ZnO with hexagonal shape (Fan *et al.*, 2007; Liu *et al.*, 2007). It has been observed that needle-shaped ZnO crystals are thermodynamically unstable and transform into nanorods (Zhang *et al.*, 2011). The ZnO seems more flower-like whereas B-doped ZnO samples consist of microrods aligned in random orientation. The morphology of X2 is similar to that of X1, pure ZnO. It can be seen that increasing the B concentration in ZnO creates larger blocks and the tips of the rods appear more broken.

The Zn  $K$ -edge absorption spectra of the samples were measured in transmission mode at ambient temperature. For a better understanding of the effect of B doping on the electronic structure of ZnO, the normalized Zn  $K$ -edge XANES spectra of ZnO are firstly compared with Zn foil, which is metallic, presented in Fig. 4(a). The spectra of ZnO and doped ZnO with different B concentrations are shown in Fig. 4(b) for comparison. Here, the expected chemical shift towards higher X-ray energies for ZnO compared with Zn is observed. Visual inspection also shows that the white line of Zn is broader than the white line of ZnO, revealing the ionic bond nature in ZnO. This effect or narrowing the white line is reversed when the ZnO is doped with B. The ZnO:B samples have a broader white line than the pristine ZnO, revealing the transformation towards a more covalent bonding in the ZnO:B, which makes it more suitable as a transparent conducting oxide. The route for the excited core electrons ( $1s$ ) of the zinc atoms that can be traceable on the Zn  $K$ -edge absorption spectra, which is dominated by the transition of the Zn  $1s$  core electrons, is to the unoccupied  $4p$  states of the conduction band. The observed characteristic peaks on the main absorption edge are referred to as the Zn  $1s \rightarrow 4p$  transitions. Metal Zn atoms have fully occupied  $3d$  levels that are pushed below the Fermi level. However, the oxides of the zinc atoms have electrons used for bonding and cause unoccupied states in the  $3d$  levels,  $Zn^{2+}$ . So, one might think that an electron excited from the core levels should have a final state in the  $d$ -levels. But, the  $1s$  to  $3d$  transition is forbidden due to quantum selection rules, which forbids  $s$  electrons relocating in  $d$  shells, *i.e.*  $\Delta l = \pm 1$ . In Fig. 4(a), the absorption spectra of the samples are given along with calculated spectra which were used for the analysis and

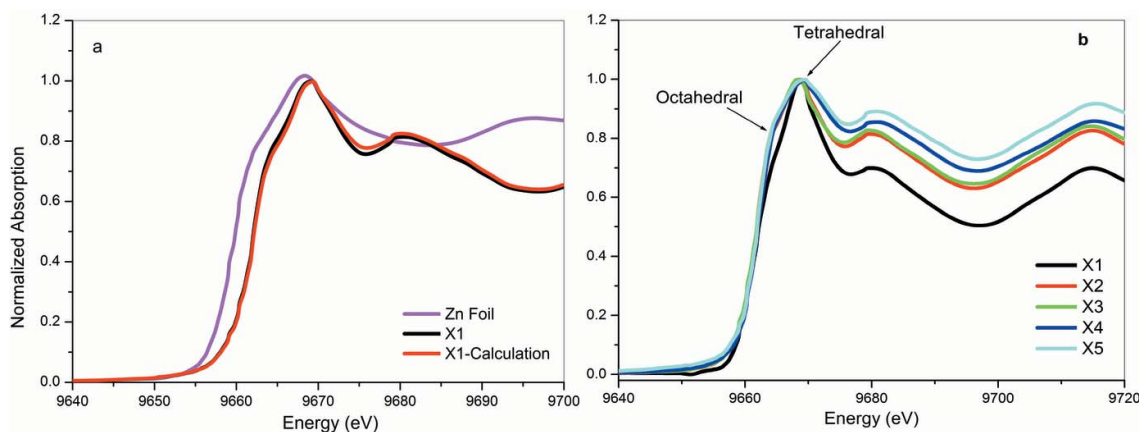


**Figure 4**  
XANES spectra at the Zn  $K$ -edge. Comparisons of (a) the Zn foil, ZnO measurement and the ZnO calculation, and (b) the ZnO and the B-doped ZnO.

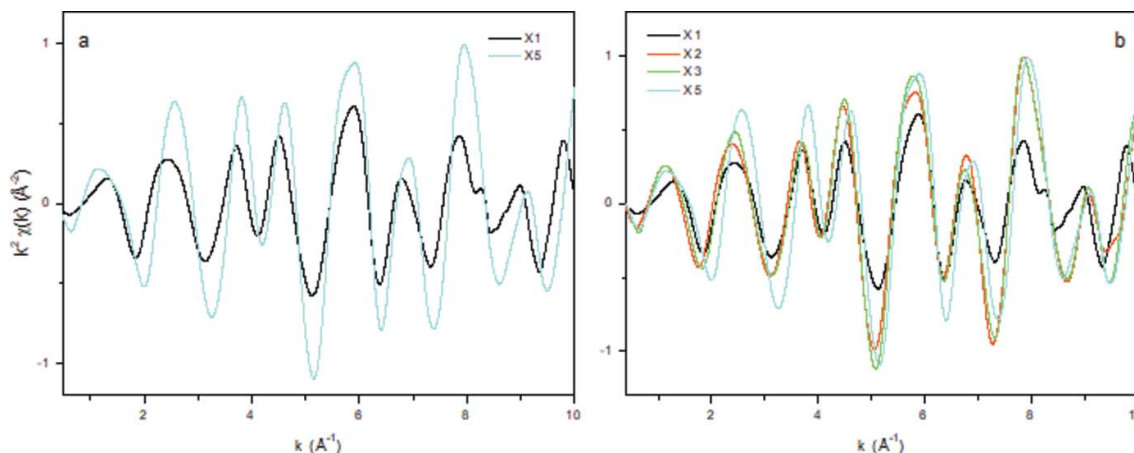


**Figure 5**  $k^2$ -weighted EXAFS spectra comparison of (a) ZnO and ZnO:B (the highest B concentration) and (b) ZnO and ZnO:B (different B concentrations).

fits. All spectral features in Fig. 4 have a high agreement in terms of the absorption edges and have a smooth rise at 9651.2 eV. Apart from Zn foil ( $Zn^0$ ), a weak pre-edge is observed at around 9653.7 eV on the ZnO spectra, which originates from hybridization of O  $2p$  and  $Zn^{2+}$   $3d$  orbitals. Metal zinc ( $Zn^0$ ) has a larger molecular band structure than the other materials, where all  $d$  levels are occupied. However, the oxide forms of the zinc have molecular bands with narrower  $4p$  levels, where the nearest neighbors are the oxygen atoms. The outer-shell electrons of oxygen are localized at the  $2p$  levels, and the unoccupied levels on zinc atoms are the  $4p$  levels. Quantum selection rules cause an impulse between the  $p$ -levels that cause narrower  $4p$  levels in the zinc oxide materials, *i.e.*  $Zn^{2+}$ . Two powerful and characteristic peak structures of the main absorption edge at 9662 eV and 9668.4 eV (9667.8 eV for Zn foil) are attributed to the Zn atoms having octahedral and tetrahedral site symmetry of ZnO. Fig. 4(b) shows a comparison of ZnO and ZnO:B spectra. No pre-edge feature is observed on the B-doped ZnO spectra. We conclude that the B-doping process affects the structural integrity to an extent that the weakly built molecular bands between Zn and O can partially fail, and break. Besides, B-doping creates a shift of around 0.7 eV towards higher energy and the main absorption-edge peaks of B-doped ZnO samples are observed at 9669.5 eV. As mentioned for ZnO above, the octahedral and tetrahedral site symmetry of ZnO:B are similar to that of ZnO and Zn foil. The doped materials have a peak at 9681 eV, which is due to multiple scattering effects of the photoelectrons in the neighboring atoms environment.

Actually, the result of the molecular interplays can be best observed in the electronic structure and in the atomic arrangements. To observe the effect of the doping processes in the crystal environment of the Zn atoms, the best tool is EXAFS spectroscopy. The EXAFS ranges approximately 50–80 eV above the main absorption edge and along the energy range 400–800 eV as the tail part of the spectra, which often exhibit the EXAFS oscillations. These oscillations are the result of scattering and interference of the emitted photo-

electron waves that are excited from their source atoms with high kinetic energies. With high kinetic energy, the photoelectrons can travel among their neighboring atoms, and the outer-shell electrons of the neighboring atoms apply a Coulombic impulse to the incoming photoelectrons, and they subsequently follow a trajectory, which is known as single- or multiple-scattering. The fluctuating data on the tail part of the spectra can be extracted by using the *ATHENA* and *ARTEMIS* programs. Fig. 5 shows the EXAFS data of the parent ZnO and ZnO:B (X5, the highest B concentration).

According to Fig. 5(a), a synchronous data fluctuation up to  $k = 8 \text{ \AA}^{-1}$  values points out that for the dominant ZnO structure at longer distances the space is occupied by Zn and O atoms. However, slight phase shifts in the scattering data beyond  $k = 8 \text{ \AA}^{-1}$  indicate a tiny disturbance on the atoms at closer distances to the source Zn atoms (*i.e.*  $k \simeq 1/\lambda$ ) doping that perturbs the trajectory of the photoelectrons.

To estimate the exact atomic locations via the distances of the atoms from the source Zn atoms on a one-dimensional axis, where the source Zn atom sits at the origin, the Fourier transform of the scattering data should be processed. The radial distribution function (RDF) data of the doped samples are given for comparison in Fig. 6. The parent sample (X1) and X5 (ZnO and ZnO:10%B) are shown in the same figure as a guide to clarify the differences in the atomic positions.

An observable shift at the oxygen peak positions points out a disturbance in the atomic locations and highlights a displacement of the host elements of the ZnO materials in their wurtzite crystal structure with increasing B doping. A comparison of the doped samples is given in Fig. 7; all samples have slight shifts as a result of the B doping.

The atomic distances in the wurtzite ZnO crystal from the source Zn atoms are given with their degeneracy as a result of the fit analysis in Table 2.

As shown in Table 2, the atomic distances in ZnO are clear. But, the exact positions where the doped B atoms are located in the crystal are still unclear. However, the shift at the scattering intensities in Fig. 6 give clues about the possible atomic placement of the doped B atoms, where O atoms peaks shift

**Table 2**

Atomic distances from the source Zn atom in the wurtzite ZnO sample.

Crystal	Coordination	Radial distance $R$ (Å) <sup>†</sup>	Degeneracy	Geometry	Space group
ZnO	Zn–O	1.83	1	Hexagonal	$P6_3mc$
	Zn–O	2.05	3		
	Zn–Zn	3.25	12		
	Zn–O	3.73	6		
	Zn–O	3.84	3		
	Zn–Zn	4.60	6		
	Zn–O	4.76	6		
	Zn–O	4.86	3		
	Zn–O	5.03	6		
	Zn–Zn	5.31	2		
	Zn–Zn	5.63	18		
	Zn–O	5.85	3		
Zn–O	5.92	6			

<sup>†</sup> Possible margin of error according to the calculated location,  $R = R \pm 0.02$  Å.

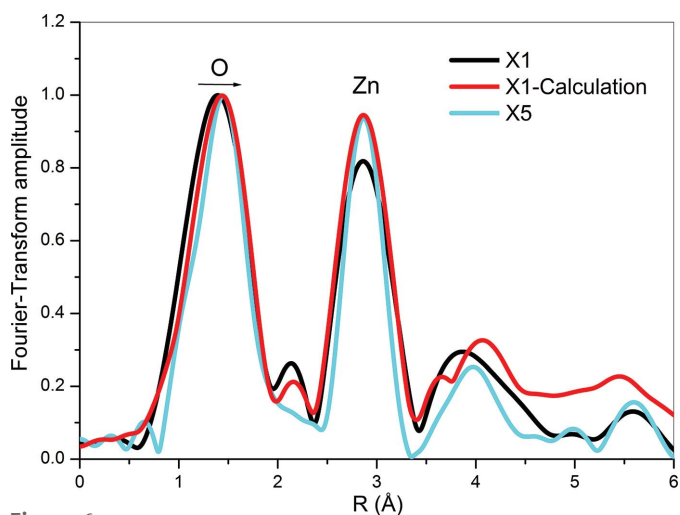


**Figure 6** Comparison of the Fourier-transform amplitude of the EXAFS spectra for the wurtzite ZnO, calculated ZnO and X5 (ZnO with highest B concentration).

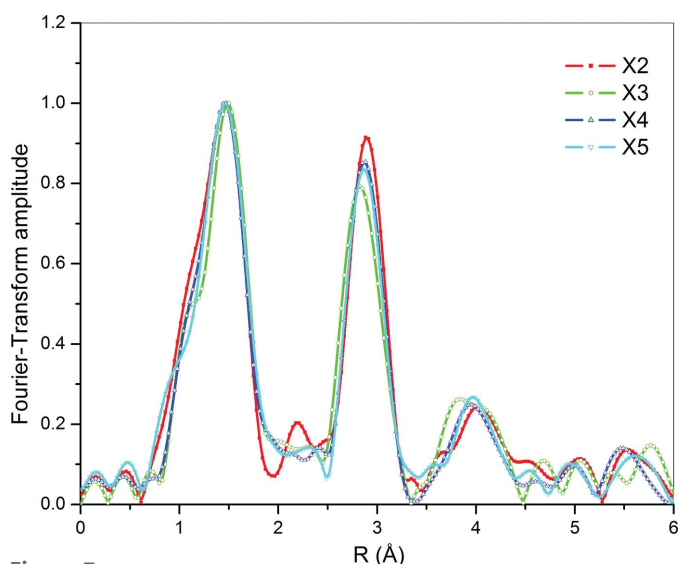


**Figure 7** Comparison of the Fourier-transform amplitude of the EXAFS spectra depending on the B concentration in ZnO.

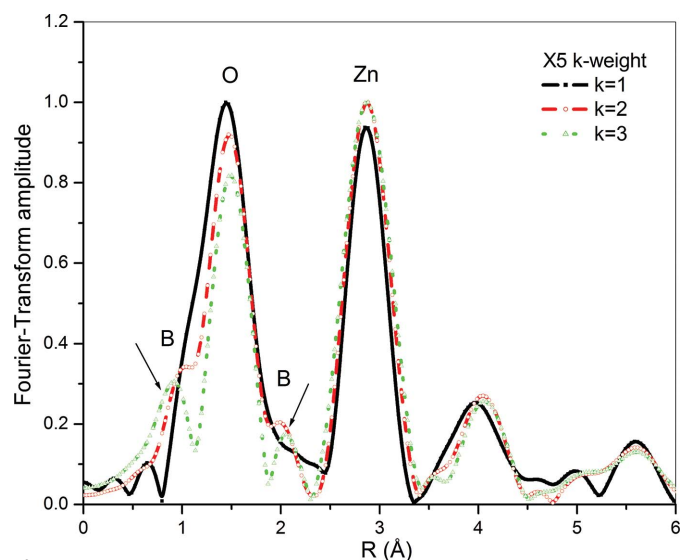


**Figure 8** The  $k$ -weight analysis for X5 (ZnO with the highest B concentration) compared in normalized style.

in opposite directions from the source Zn atom. A possible technique from the EXAFS study can give us the exact distance of the boron atoms from the zinc atoms in the crystal structure. Results from a ‘ $k$ -weight’ study on the X5 material are given in Fig. 8. Using the  $k$ -weight technique, the RDF data are multiplied by the powers of  $k$  causing differences in the peak features due to the different types of atoms, both in weight and location, which have overlapping signals.

The  $k$ -weighted data allow the separation of heavy and light atoms in the measured data, determination of different peaks in the overlapped spectra, and have asymmetry (shift) in the presence of different atoms when normalized. In Fig. 8, despite normalization, the X5 data show no shift. Thus, the true positions of the Zn and O atoms can be distinguished by looking at their peak intensities. Here, the overlapping data of the oxygen atoms located between the absorbing Zn atom at the origin and the Zn atoms at a distance of 3.25 Å can be seen more clearly with their large peak structures. The weak peak structure between Zn and O atoms, which does not break the symmetry despite the decay of the normalized data, emphasizes that there is a small atom at this point. The two peaks are attributed to the doped B atoms sitting at 1.03 Å and 2.18 Å between the O and Zn atoms. These analysis results have a high agreement with both the scattering and the XRD pattern results.

### 5. Conclusions

The electronic and crystallographic structure of ZnO and ZnO:B powders synthesized by hydrothermal method have been investigated using XRD and XAFS (NEXAFS and EXAFS) techniques. Zn<sup>0</sup> has a larger molecular band structure, where all  $d$  levels are occupied, whereas the oxide form of Zn, in which the nearest neighbors are O atoms, has narrower  $4p$  molecular bands. The high symmetry in B-doped ZnO samples emphasizes that B has no destructive influence

on the crystallographic structure of ZnO. In other words, ZnO:B samples keep the wurtzite hexagonal structure with space group  $P6_3mc$  confirmed by XRD results, which are supported by the EXAFS results. The atomic distances from the Zn atom in the wurtzite structure of ZnO are accurately calculated using EXAFS data. The radial distances of Zn–O with a degeneracy of 6 are 3.73 Å, 4.76 Å, 5.03 Å and 5.92 Å. In addition, the Zn–Zn distance is 4.60 Å for the same degeneracy. Although it is relatively difficult to define the position of a light atom in the crystal structure, in the present research the position of the B atom in the ZnO is defined using a detailed EXAFS study with  $k$ -weight analysis of the samples. The  $k$ -weight analysis revealed that B atoms are located in between the Zn and O atoms at 1.03 Å and 2.18 Å closer to the O atoms. SEM images show that ZnO and ZnO:B are grown in micrometre-scale rods of hexagonal shape; some of them are needle-shaped. Increasing the concentration of B in ZnO affects the morphology, which led us to suggest that the number of the broken/destroyed rods is increased. We conclude that the B atoms, which can mainly be found between the Zn and O atoms, weaken and/or break the Zn–O bonds resulting in more broken rods on the microscopic scale.

### Funding information

Financial support from Mersin University Scientific Research Projects Unit (BAP) Project No. 2019-1-AP4-3197 and Project No. 2019-1-AP5-3438 is acknowledged. Financial support from the Richard Lounsbery Foundation for the SESAME Users program 20185055 is also acknowledged.

### References

Allisson, F. (1930). Thesis, ETH Zürich, Switzerland.  
 Ankudinov, A. L. & Rehr, J. J. (1997). *Phys. Rev. B*, **56**, R1712–R1716.  
 Bagnall, D. M., Chen, Y. F., Zhu, Z., Yao, T., Shen, M. Y. & Goto, T. (1998). *Appl. Phys. Lett.* **73**, 1038–1040.  
 Baruah, S. & Dutta, J. (2009). *Sci. Technol. Adv. Mater.* **10**, 013001.  
 Baur, E. & Neuweiler, C. (1927). *Helv. Chim. Acta*, **10**, 901–907.  
 Braun, A. (2017). *X-ray Studies on Electrochemical Systems – Synchrotron Methods for Energy Materials*. De Gruyter.  
 Chiou, J. W., Jan, J. C., Tsai, H. M., Bao, C. W., Pong, W. F., Tsai, M., Hong, I., Klauser, R., Lee, J. F., Wu, J. J. & Liu, S. C. (2004a). *Appl. Phys. Lett.* **84**, 3462–3464.  
 Chiou, J. W., Kumar, K. P. K., Jan, J. C., Tsai, H. M., Bao, C. W., Pong, W. F., Chien, F. Z., Tsai, M., Hong, I., Klauser, R., Lee, J. F., Wu, J. J. & Liu, S. C. (2004b). *Appl. Phys. Lett.* **85**, 3220–3222.  
 Du, X., Mei, Z., Liu, Z., Guo, Y., Zhang, T., Hou, Y., Zhang, Z., Xue, Q. & Kuznetsov, A. Y. (2009). *Adv. Mater.* **21**, 4625–4630.  
 El-Hilo, M., Dakhel, A. A. & Ali-Mohamed, A. Y. (2009). *J. Magn. Mater.* **321**, 2279–2283.  
 Ellmer, K. & Fiechter, S. (2008). *Phys. Status Solidi B*, **245**, 1743–1744.  
 Erat, S. & Yildirimcan, S. (2019a). *Turk. J. Eng.* **3**, 43–50.  
 Erat, S. & Yildirimcan, S. (2019b). *Turk. J. Eng.* **3**, 68–75.  
 Fan, L., Song, H., Yu, L., Liu, Z., Yang, L., Pan, G., Bai, X., Lei, Y., Wang, T., Zheng, Z. & Kong, X. (2007). *Opt. Mater.* **29**, 532–538.

Harfouche, M., Abdellatif, M. & Paolucci, G. (2018). *Proceedings of the 17th International Conference on X-ray Absorption Fine Structure (XAFS2018)*, 22–27 July 2018, Kraków, Poland.  
 Heiland, G. (1981). *Sens. Actuators*, **2**, 343–361.  
 Jeong, E., Yu, H., Han, S., An, S. J., Yoo, J., Kim, Y. & Yi, G. (2008). *J. Kor. Phys. Soc.* **53**, 461–465.  
 Kumar, V., Singh, R. G., Purohit, L. P. & Mehra, R. M. (2011). *J. Mater. Sci. Technol.* **27**, 481–488.  
 Kuthirummal, N., Smith, G. M., Lopez, L., Podila, R., Howell, J., Dun, C. & Rao, A. M. (2016). *AIP Adv.* **6**, 095225.  
 Law, M., Greene, L. E., Johnson, J. C., Saykally, R. & Yang, P. (2005). *Nat. Mater.* **4**, 455–459.  
 Liu, G., Wang, L. & Zhou, J. (2007). *Ferroelectrics*, **356**, 225–229.  
 Look, D. C., Reynolds, D. C., Fang, Z., Hemsley, J. W., Sizelove, J. R. & Jones, R. L. (1999). *Mater. Sci. Eng. B*, **66**, 30–32.  
 Martinson, A. B., Elam, J. W., Hupp, J. T. & Pellin, M. J. (2007). *Nano Lett.* **7**, 2183–2187.  
 Meyers, J., Anderson, J. T., Hung, C. M., Thompson, J., Wager, J. F. & Keszler, D. A. (2008). *J. Am. Chem. Soc.* **130**, 17603–17609.  
 Momma, K. & Izumi, F. (2011). *J. Appl. Cryst.* **44**, 1272–1276.  
 Norton, D. P. (2004). *Mater. Sci. Eng. Rep.* **43**, 139–247.  
 Núñez-Salas, R. E., Hernández-Ramírez, A., Hinojosa-Reyes, L., Guzmán-Mar, J. L., Villanueva-Rodríguez, M. & Maya-Treviño, M. L. (2019). *Catal. Today*, **328**, 202–209.  
 Ozkendir, O. M., Harfouche, M., Ulfat, I., Kaya, C., Celik, G., Ates, S., Aktas, S., Bavegar, H. & Colak, T. (2019). *J. Electron Spectrosc. Relat. Phenom.* **235**, 23–28.  
 Pawar, P., Cai, G., Ham, D., Mane, R. S., Ganesh, T., Ghule, A., Sharma, R., Jadhava, K. D. & Han, S. (2009). *Solar Energy Mater. Solar Cells*, **93**, 524–527.  
 Ravel, B. (2001). *J. Synchrotron Rad.* **8**, 314–316.  
 Ravel, B. & Newville, M. (2005). *J. Synchrotron Rad.* **12**, 537–541.  
 Romeiro, F. C., Marinho, J. Z., Lemos, S. C. S., de Moura, A. P., Freire, P. G., da Silva, L. F., Longo, E., Munoz, R. A. A. & Lima, R. C. (2015). *J. Solid State Chem.* **230**, 343–349.  
 Saleh, R. & Djaja, N. F. (2014). *Spectrochim. Acta A Mol. Biomol. Spectrosc.* **130**, 581–590.  
 Senol, S. D., Ozturk, O. & Terzioğlu, C. (2015). *Ceram. Int.* **41**, 11194–11201.  
 Šipr, J. & Rocca, F. (2011). *J. Phys. Condens. Matter*, **23**, 315501.  
 Steinhäuser, J., Faÿ, S., Oliveira, N., Vallat-Sauvain, E. & Ballif, C. (2007). *Appl. Phys. Lett.* **90**, 142107.  
 Steinhäuser, J., Faÿ, S., Oliveira, N., Vallat-Sauvain, E., Zimin, D., Kroll, U. & Ballif, C. (2008). *Phys. Status Solidi A*, **205**, 1983–1987.  
 Tahar, J. & Tahar, N. B. H. (2005). *J. Mater. Sci.* **40**, 5285–5289.  
 Tributsch, H. (1968). Thesis, Technische Universität München, Germany.  
 Tributsch, H. (1969). *Ber. Bunsenges. Phys. Chem.* **73**, 582–590.  
 Tsay, C. & Hsu, W. (2013). *Ceram. Int.* **39**, 7425–7432.  
 Tsuzuki, T., He, R., Dodd, A. & Saunders, M. (2019). *Nanomaterials*, **9**, 481.  
 Wang, J., Yang, J., Han, N., Zhou, X., Gong, S., Yang, J., Hu, P. & Chen, Y. (2017). *Mater. Des.* **121**, 69–76.  
 Wang, W., Ai, T. & Yu, Q. (2017). *Sci. Rep.* **7**, 42615.  
 Xu, X. G., Yang, H. L., Wu, Y., Zhang, D. L., Wu, S. Z., Miao, J., Jiang, Y., Qin, X. B., Cao, X. Z. & Wang, B. Y. (2010). *Appl. Phys. Lett.* **97**, 232502.  
 Yildirimcan, S., Ocakoglu, K., Erat, S., Emen, F. M., Repp, S. & Erdem, E. (2016). *RSC Adv.* **6**, 39511–39521.  
 Zargar Shoushtari, M., Poormoghadam, A. & Farbod, M. (2017). *Mater. Res. Bull.* **88**, 315–319.  
 Zhang, P., Lee, T., Xu, F. & Navrotsky, A. (2008). *J. Mater. Res.* **23**, 1652–1657.